Electronic structure analysis of the Diels-Alder cycloaddition catalyzed by alkali-exchanged faujasites

Please check the document version of this publication:

• A submitted manuscript is the version of the article upon submission and before peer-review. There can be important differences between the submitted version and the official published version of record. People interested in the research are advised to contact the author for the final version of the publication, or visit the DOI to the publisher's website.
• The final author version and the galley proof are versions of the publication after peer review.
• The final published version features the final layout of the paper including the volume, issue and page numbers.

Link to publication

Electronic Structure Analysis of the Diels−Alder Cycloaddition Catalyzed by Alkali-Exchanged Faujasites

Roderigh Y. Rohling,[†,§] Ionut C. Tranca,[‡,§] Emiel J. M. Hensen,*[†] and Evgeny A. Pidko*[†,‖]

[†]Inorganic Materials Chemistry group, Department of Chemical Engineering, and [‡]Energy Technology, Department of Mechanical Engineering, Eindhoven University of Technology, P.O. Box 513, 5600 MB, Eindhoven, The Netherlands

S *Supporting Information*

ABSTRACT: The Diels−Alder cycloaddition (DAC) reaction is a commonly employed reaction for the formation of C−C bonds. DAC catalysis can be achieved by using Lewis acids and via reactant confinement in aqueous nanocages. Low-silica alkali-exchanged faujasite catalysts combine these two factors in one material. They can be used in the tandem DAC/dehydration reaction of biomass-derived 2,5-dimethyl-furan (DMF) with ethylene toward *p*-xylene, in which the DAC reaction step initiates the overall reaction cycle. In this work, we performed periodic density functional theory (DFT) calculations on the DAC reaction between DMF and C_2H_4 in low-silica alkali(M)-exchanged faujasites (MY; Si/Al = 2.4; M = Li^+, Na^+, K^+, Rb^+, Cs^+). The aim was to investigate how confinement of reactants in MY catalysts changed their electronic structure and the DAC-reactivity trend among the evaluated MY zeolites. The conventional high-silica alkali-exchanged isolated site model (MFAU; Si/Al = 47) served as a reference. The results show that confinement leads to initial-state (IS) destabilization and transition-state (TS) stabilization. Among the tested MY, most significant IS destabilization is found in RbY. Only antibonding orbital interactions between the reactants/reactive complex and cations were found, indicating that TS stabilization arises from ionic interactions. Additionally, in RbY the geometry of the transition state is geometrically most similar to that of the initial and final state. RbY also exhibits an optimal combination of the confinement-effects, resulting in having the lowest computed DAC-activation energy. The overall effect is a DAC-reactivity trend inversion in MY as compared to the trend found in MFAU where the activation energy correlates with the Lewis acidity of the exchangeable cations.
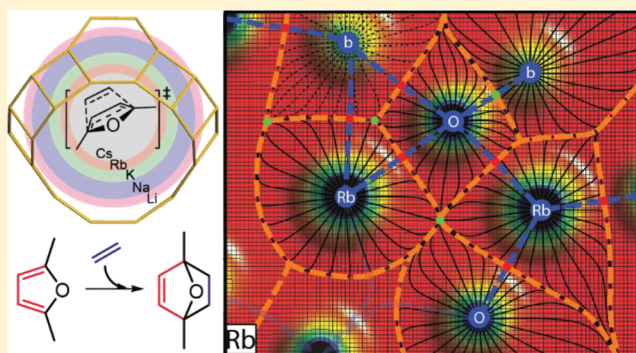
1. INTRODUCTION

The Diels−Alder cycloaddition[1] (DAC) is a widely used synthetic methodology for constructing new carbon−carbon bonds.[2−6] It is a pericyclic reaction in which a 1,3-conjugated diene couples with a dienophile possessing a double or a triple bond. The mechanism of the DAC reaction involves a concerted bond formation in the transition state. Depending on the electronic structure of the reactants, this can happen either synchronously or asynchronously if the nascent bonds are of equal or unequal length, respectively.[7] If either of the reactants is highly activated, the reaction can proceed via a two-step mechanism characterized by the formation of an intermediate (I) with one C−C bond formed.[8,9]

The reaction proceeds through the formation of a transition state in which the frontier molecular orbital[10−14] (FMO) symmetries need to be conserved, a requirement that led to the formulation of the Woodward−Hoffmann rules. These selection rules aid in assessing whether the reaction is symmetry forbidden (e.g., ethylene−ethylene, [2 + 2] cycloaddition) or allowed (e.g., ethylene−1,3-dibutadiene, [4 + 2] cycloaddition) and allow determination of the final stereochemistry of the product.[15,16] Furthermore, a propor-

tionality has been proposed between the DAC-activation barrier and the energy and symmetry of the highest-occupied-molecular-orbital (HOMO) and the lowest-unoccupied-molecular-orbital (LUMO) of the reactants.[13,14,17,18] Three mechanisms are distinguished based on these energy levels, being the normal, inverse, and the neutral electron demand mechanisms. A schematic representation of the first two mechanisms is shown in Figure 1a. The normal electron demand mechanism is related to the normal energy gap (e_{norm}): $|HOMO_{diene} − LUMO_{dienophile}|$. The inverse electron demand mechanism is related to the inverse energy gap (e_{inv}): $|LUMO_{diene} − HOMO_{dienophile}|$. The third is the neutral electron demand mechanism in which $e_{norm} = e_{inv}$.

Narrowing the energy gap can be achieved through introduction of substituents to the reactants.[9,14,17,19−21] Such substituents can be either electron-donating groups (EDG) or electron-withdrawing groups (EWG). Addition of an EDG to the diene increases the $HOMO_{diene}$, while the introduction of
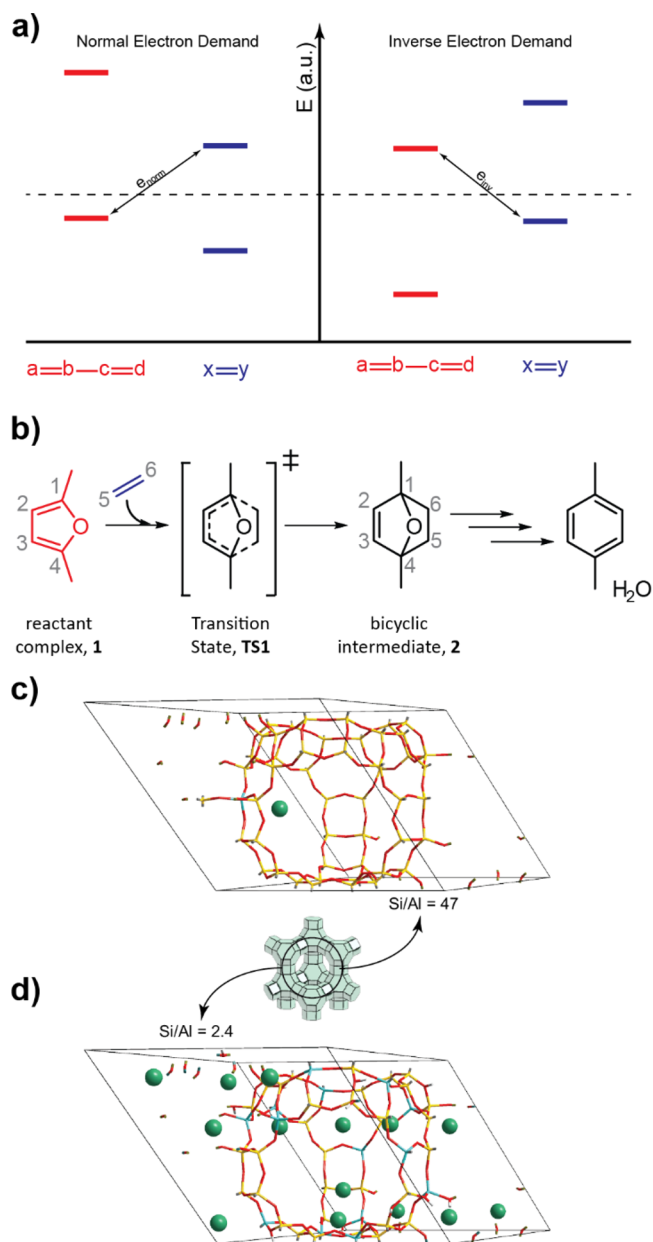
Figure 1. (a) Schematic representation of the frontier molecular orbital energy levels in the normal electron demand and inverse electron demand mechanisms. (b) The Diels−Alder cycloaddition between DMF and ethylene as the first step in the overall DAC/D reaction toward *p*-xylene. (c) The conventional alkali-exchanged faujasite model with an isolated site. (d) The low-silica alkali-exchanged faujasite model with high accessible site density.

an EWG to the dienophile lowers the $LUMO_{dienophile}$. An alternative method to accelerate the DAC reaction involves the use of Lewis acid catalysts, which are essentially EWGs.[22−24]

Apart from altering the electronic structure of the reactants by substituents or Lewis acids, the DAC reaction can also be catalyzed by confinement. Supramolecular complexes,[25,26] enzymes,[27−30] and the liquid phase[31−35] are some illustrative examples of systems exhibiting confinement-driven catalysis of the DAC reaction. In supramolecular complexes, the specific molecular fit biases one reaction channel leading to high product-selectivity.[25,26] Although only relatively few Diels− Alderases are known, enzymatic catalysis[27−30] is characterized

by both reactant prealignment and electrostatic and/or hydrophobic transition state stabilization. Lastly, liquid phase catalysis, sometimes termed "on-water catalysis",[31−35] is another example of confinement-driven reactivity. In this scenario, reactants experience a hydrophobic effect that pushes the reactants together in an aqueous nanocage accompanied by the subsequent stabilization of the transition state via hydrogen bonding.

Recently, we studied low-silica alkali-exchanged faujasite zeolite catalysts (MY, Si/Al = 2.4; M = Li$^+$, Na$^+$, K$^+$, Rb$^+$, Cs$^+$) in the one-pot Diels−Alder cycloaddition (DAC)/dehydration (D) reaction of 2,5-dimethylfuran (DMF) with ethylene for *p*-xylene production, Figure 1b.[36] These faujasite catalysts contain many accessible Lewis acid sites in the confined hydrophilic space of the faujasite supercage. Although KY proved to be the best catalyst for the overall reaction, RbY possessed the lowest DAC reaction barrier. The latter observation was surprising, because the lowest DAC reaction barrier was not expected for one of the weakest Lewis acids. Furthermore, the DAC-reactivity trend was also found to be insensitive to changes of the substituents when changing DMF to either furan or furandicarboxylic acid.[37]

It is known that substrate confinement in the micropores of cation-exchanged zeolites gives rise to perturbation of the substrate's electronic structure, e.g. intermolecular orbital overlap in alkene photo-oxidation chemistry[38] or changes in CO IR-stretching vibrations due to dual- and multisite adsorption modes.[39] Recently, computational studies using a combination of electronic structure analysis techniques have led to an improved understanding of reactivity and scaling laws on transition metal surfaces,[40,41] transition metal oxides,[42] and zeolites.[43] Among the applied methods were the density-derived electrostatic and chemical (DDEC) method,[44−46] the crystal orbital hamilton population (COHP) analysis,[47−51] and crystal orbital overlap population (COOP) analysis.[52] By complementing the above methods with the topological analysis of the electron density in conformity with the quantum theory of atoms in molecules (QTAIM),[53−57] we expect to elucidate the origin of catalysis of the DAC reaction by the MY systems.

Herein we report on an in-depth electronic structure analysis of the DAC reaction between DMF and ethylene over alkali-exchanged faujasites using periodic DFT calculations and a variety of electronic structure analysis tools. We establish fundamental understanding on the origin of the DAC reaction barrier trend inversion in low-silica alkali-exchanged faujasite-based catalysts. We do so by studying the conventional isolated site model and a model containing a high density of accessible active sites, Figure 1c and Figure 1d, respectively. The results show that the energy barrier is governed by confinement-induced initial-state (IS) destabilization and the cooperative action of the alkali cations in stabilizing the transition state (TS) via ionic interactions. Among the studied MY catalysts, RbY (Si/Al = 2.4) is found to exhibit an optimal combination of IS destabilization and TS stabilization.

2. COMPUTATIONAL DETAILS

2.1. Reaction Energetics and Model. Similar to our previous works,[36,37] we studied the DAC reaction between 2,5-dimethylfuran and ethylene over two types of periodic, rhombohedral faujasite models exchanged with alkali cations (M = Li$^+$, Na$^+$, K$^+$, Rb$^+$, Cs$^+$). The first model was a high-silica alkali-exchanged faujasite (Si/Al = 47, Si$_{47}$Al$_1$O$_{96}$M$_1$, MFAU)

containing a single isolated site in the faujasite supercage. The second model represented a low-silica alkali-exchanged faujasite (Si/Al = 2.4, $Si_{34}Al_{14}O_{96}M_{14}$, MY) containing a high density of accessible sites in the faujasite supercage. The placement of the cations has been described elsewhere.[36]

The periodic density functional theory (DFT) calculations using the Vienna ab-initio simulation package (VASP) were performed with the gradient corrected PBE exchange-correlation functional[58−62] and the projected-augmented-wave scheme (PAW) to describe the electron−ion interactions. Long-range dispersive interactions were accounted for by using the DFT-D3 method with Becke-Johnson damping.[63,64] The k-point mesh was limited to the gamma point only with a plane-wave basis set cutoff energy of 500 eV. Typically, a root-mean-square (RMS) force convergence criterion of 0.015 eV/Å was employed. Occasionally, some models did not fully reach this strict RMS-force criterion and the convergence criterion was relaxed to 0.035 eV/Å. The forces exceeding the original criterion originated from forces acting on cations confined within the double six-membered rings connecting the sodalite cages, but which where distant from the active site. The relaxed convergence criteria were deemed acceptable because the current zeolite models feature extremely shallow potential energy surfaces. The structural optimization below 0.05 eV/Å usually leads to energy changes below 5 kJ/mol.

The transition state was identified utilizing a two-step procedure. First, a climbing-nudged-elastic band (CNEB) calculation[65,66] was performed to estimate the minimum energy pathway (MEP) (5 eV/Å^2 spring constant, maximum length hypervector between images 0.5 Å). The accepted RMS force of the converged CNEB was 0.14 eV/Å or lower. Consecutively, geometry optimization of the identified transition state was continued using the quasi-Newton procedure (max. RMS < 0.015 eV/Å). To confirm the nature of the stationary point, we used the finite displacement method to compute the vibrational frequencies.

2.2. Electronic Structure Analysis. Bond orders, net atomic charges, the electron density, and Laplacian values at the bond critical points (BCPs), as well as the partial density of states (pDOS), crystal orbital Hamiltonian population (COHP), and crystal orbital overlap population (COOP) functions, were investigated (Supporting Information S1.1−S1.3).

2.3. Atomic Net Charges and Bond Critical Point Analysis. The atomic charges were computed according to the methods described by the Austin group[53−56] (Supporting Information S1.1.). Net atomic charges were obtained by referencing the charges against the ideal valence charge of every atom species. An in-house written script and freely available software[67,68] were used to analyze and visualize the topology of the electron density in conformity with the QTAIM theory.[53−57] Bond-critical points (BCPs) were assigned to saddle-points along the bond-paths. The Laplacian at a BCP was used to characterize the nature of the pairwise interaction, providing insight into the covalent/ionic character of a bond. A negative value of the Laplacian is indicative of a covalent bond, while a positive Laplacian indicates noncovalent bonds such as an ionic bond, hydrogen bond, or van der Waals interaction.[69]

2.4. Bond Orders. Bond orders (BO) were analyzed using the Chargemol code. We refer to the literature for extensive derivation of the equations necessary to both compute the bond orders and execute the underlying DDEC6-based charge partitioning.[44−46] Briefly, the bond order of an atom pair A (in the unit cell) and j (atoms in both unit cell and periodic images) is described with eq 1:

$$B_{A,j} = CE_{A,j} + \Lambda_{A,j} \tag{1}$$

where $B_{A,j}$ is the bond order between atom A and j, $CE_{A,j}$ is the contact exchange, and $\Lambda_{A,j}$ is the dressed exchange hole delocalization term. The term $CE_{A,j}$ describes the electron exchange between atoms A and j in a material, formulated in eq 2:

$$CE_{A,j} = 2 \oint \frac{\vec{\rho}_A^{avg}(\vec{r}_A) \cdot \vec{\rho}_j^{avg}(\vec{r}_j)}{\bar{\rho}^{avg}(\vec{r}) \cdot \bar{\rho}^{avg}(\vec{r})} \rho(\vec{r}) d^3\vec{r} \tag{2}$$

where any $\vec{\rho}_i^{avg}$ is the average spherical electron density of atom i as a function of the atomic electron distribution and atomic spin magnetization density vector obtained through DDEC6-based partitioning of the electron density. The term $\bar{\rho}^{avg}$ is the sum of all $\vec{\rho}^{avg}$ found in the material (unit cell + periodic images). Note that this equation deals with the dressed exchange hole, which is an adjusted (either more contracted or more diffuse) exchange hole to obtain more accurate bond orders. The second term in eq 1 is the dressed exchange hole delocalization term, defined according to eq 3:

$$\Lambda_{A,j} = X_{A,j}^{coord.nr.} X_{A,j}^{pairwise} X_{A,j}^{con.} \leq CE_{A,j} \tag{3}$$

where $X_{A,j}^{coord.nr.}$ accounts for coordination number effects and $X_{A,j}^{pairwise}$ for pairwise interactions, and $X_{A,j}^{con.}$ is a constraint on the density-derived localization index, $B_{A,A}$. The latter is a matrix that equals the total number of the dressed exchange electrons in the material (unit cell + periodic images). These terms are constraints and scaling relationships to keep the bond orders well-behaved.

2.5. Crystal Orbital Hamilton Population. The pDOS provides information on the electron density distribution as a function of energy. The crystal orbital Hamiltonian population is related to it and allows partitioning of the electron density distribution into bonding, nonbonding, and antibonding interaction domains (Supporting Information S1.3.).[47−51] The $-COHP_{ij}(E)$ is defined in eq 4 as

$$-COHP_{ij}(E) = H_{ij} \sum_n c_i^n c_j^n \delta(E - E_n) \tag{4}$$

where H_{ij} represents the Hamiltonian matrix element between atomic orbitals φ_i and φ_j, and c_i and c_j are the coefficients of these atomic orbitals in the molecular orbital ψ_n ($\psi_n = \sum_i c_i^n \varphi_i$). A positive value for $-COHP_{ij}(E)$ symbolizes a bonding electronic interaction between the atomic orbitals i and j, while a negative value describes an antibonding interaction. A value of zero is associated with a nonbonding interaction. The integrated value of $-COHP_{ij}(E)$, ICOHP, can be considered to be a measure for the bond strength. This formulation provides a good approximation of the bond energy as long as the repulsive energy of the nuclei is canceled by the double-counted electrostatic interactions.[70]

2.6. Crystal Orbital Overlap Population Analysis. The crystal orbital overlap population ($COOP_{ij}(E)$, Supporting Information S1.3) function introduced by Hoffmann[52] can be defined according to eq 5:

$$COOP_{ij}(E) = S_{ij} \sum_n c_i^n c_j^n \delta(E - E_n) \tag{5}$$

where $S_{ij} = \langle \varphi_i | \varphi_j \rangle$ is the overlap of atomic orbitals φ_i and φ_j. The values of $\text{COOP}_{ij}(E)$ also quantify the bonding or antibonding character of the orbital interactions, but the electron density is now weighted by the atomic orbital overlap S_{ij} instead of the bond energy overlap H_{ij}. As a consequence, $\text{COOP}_{ij}(E)$ cannot quantitatively analyze the contribution of the bonds to the total energy like the $-\text{COHP}_{ij}(E)$ does. A quantitative evaluation of the bond strengths can nevertheless be obtained from the values of the integrated COOP (in unit of electrons).

3. RESULTS

3.1. Reaction Energies. All geometries of the zeolite models, reaction intermediates, and transition states involved in the DAC reaction between DMF and C_2H_4 were adopted from our previous study.[36] A schematic representation of the reaction energy diagram is shown in Figure 2a. The
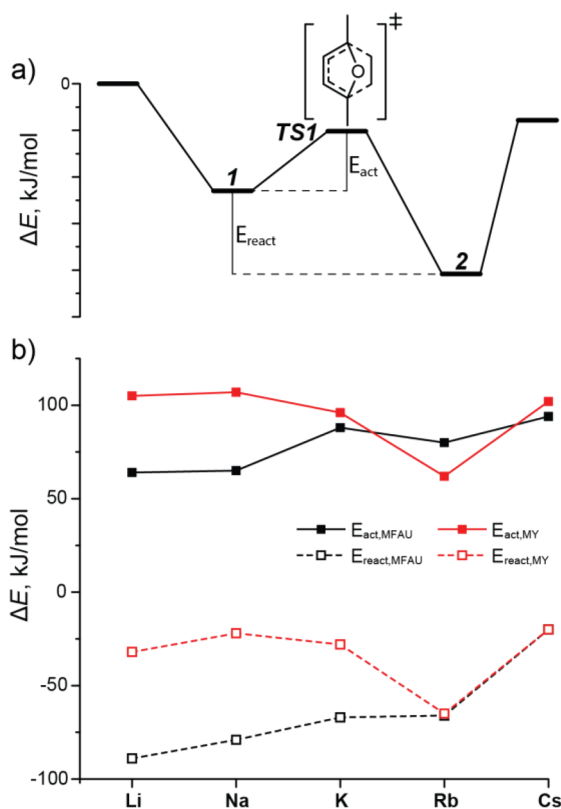

Figure 2. Schematic representation of the DAC reaction energy profile is shown in part a, illustrating the definitions of the activation and reaction energies. The changes in activation energy and the change in reaction energy as a function of the exchangeable cation in MFAU and MY are shown in part b.

dependency of the DAC activation energy (E_{act}) and the change in reaction energy (E_{react}) in the different models is given in Figure 2b. Changes to the reactant adsorption energy (E_{ads}) and E_{act} in MY are shown in Figure S1.

The coupling reaction starts from the adsorbed states **1**/MFAU or **1**/MY (e.g., DMF + C_2H_4 + MY → **1**/MY) for the single- and multiple cation-exchanged faujasite models, respectively. In both models, DMF adsorbs in a η^5-fashion to the exchangeable SII cation. In MFAU, ethylene is physisorbed and interacting with the zeolite matrix via dispersive interactions. In MY, ethylene is η^2-coordinated to a

neighboring SII cation. The DAC reaction yields the bicyclic intermediate **2** via a cyclic synchronous concerted transition state (**TS1**, $\Delta d = d(C_1 \cdots C_6) - d(C_4 \cdots C_5) < 0.04$ Å).

Previous work showed a decrease in adsorption energy with a concomitant decrease in Lewis acidity of the cations in MFAU.[36] Following adsorption, the reaction proceeds with ethylene approaching adsorbed DMF. The reaction energy decreases from -89 kJ/mol in LiFAU to -20 kJ/mol in CsFAU. As qualitatively expected for single Lewis acid catalysis, E_{act} increases with decreasing Lewis acidity from 64 kJ/mol in LiFAU to 94 kJ/mol in CsFAU, attributed to Cs^+ being the weakest Lewis acid among the evaluated alkali cations. E_{act} in KFAU deviates from the expected trend of increasing activation energy with decreasing Lewis acidity, explained elsewhere.[37]

In the MY models, the reaction cycle starts with coadsorption of the reactants. The adsorption is generally weaker for the weaker Lewis acids. Note that the E_{ads} of the individual compounds generally add up to the energy of the coadsorbed state **1**/MY. This is, however, not the case in RbY ($E_{1/RbY} = -88$ kJ/mol vs $E_{ads,sum} = E_{ads,DMF} + E_{ads,ethylene} = -111$ kJ/mol). With increasing cation radius, the interatomic $C_4 \cdots C_5$ and $C_1 \cdots C_6$ distances gradually decrease from ca. 5.6 to 3.5 Å for LiY to RbY, respectively. The size of the Cs^+ cations causes DMF and ethylene to be 3.8 Å apart. In MY systems, the trend in E_{act} is inverted as compared to the MFAU systems. The highest barriers are now found for the strongest Lewis acids (Li^+, Na^+; $E_{act} = 105$ and 107 kJ/mol, respectively) and the lowest barrier for one of the weakest Lewis acids (Rb^+, $E_{act} = 62$ kJ/mol).

The changes to the reaction energies are investigated by correlating the change in E_{act} with the change in E_{react} for MFAU- and MY-based models, Figure 2b. We find a qualitative agreement between E_{act} and E_{react} for both models. Although not conclusive, this might hint at a resemblance of the TS to the FS. However, reaction energies alone are not sufficient to conclusively support this statement.

To conclude our study on the reaction energies, we investigated possible (co)adsorption effects on the activation barrier height in the MY models. The obtained trend shows that the activation energy does not correlate well with the (cumulative) adsorption energy (Figure S1). While we find the DMF adsorption energy to decrease with ca. 65 kJ/mol from LiY to KY, the activation energy only decreases with about 10 kJ/mol. Furthermore, the trend in E_{act} shows a minimum for RbY and sharply increases for CsY. If the activation barrier would be governed by the adsorption energy, one would also expect a low barrier for CsY.

In summary, the computed reaction energies indicate that formation of the TS is made easier by IS-destabilization in RbY as compared to the other modeled MY catalysts. However, the qualitative relation between E_{react} and E_{act} rule IS-destabilization out to be the only factor.

3.2. Alkali Cation Influence on the Energy Gaps. Next, we investigated a possible relation between changing activation barrier and Lewis acid catalysis by the various alkali cations. To that end, we computed the pDOS for every initial state in MFAU and MY. We also computed the degree of orbital overlap of the cations with the furanic oxygen atom (O_{DMF}) and DMF carbon backbone.

The pDOS of DMF, ethylene, and the five accessible cations is presented in Figure 3. Note that we have omitted the contributions of the hydrogen 1s-orbitals. These orbitals only
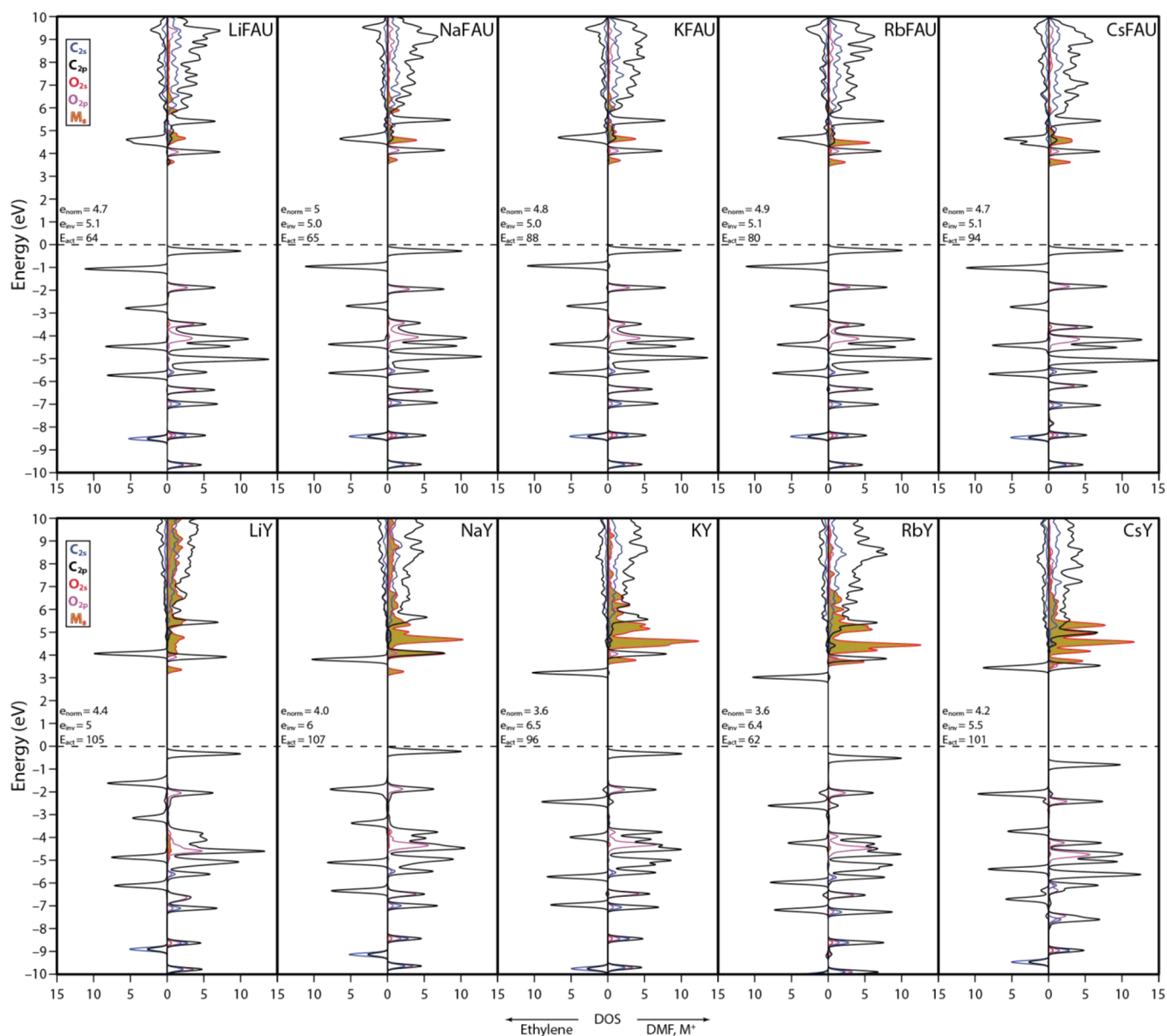
Figure 3. PDOS of the MFAU catalysts (top row) and the MY catalysts (bottom row). The Fermi level is located at 0 eV. Every panel is a separate catalyst. Within every panel, the DOS of ethylene is plotted to the left and that of DMF and the cation to the right. The values of e_{norm} and e_{inv} are in eV and that of E_{act} in kJ/mol.

increase the intensity of the bands and do not give rise to new bands. The values of e_{norm}, e_{inv}, and E_{act} relevant to the pDOS of the cation in the panel are displayed too. Examples of COOP plots are shown in Figure S2 (NaY and RbY). These are representative examples for all other MY and illustrate the type of orbital interactions.

Inspection of Figure 3 shows that e_{norm} and e_{inv} in MFAU vary only little for the different cations. Meanwhile, the activation energy increases with decreasing Lewis acidity. For instance, e_{norm} (e_{inv}) is 4.7 (5.1) eV in LiFAU with an activation barrier of 64 kJ/mol, while those in CsFAU are 4.7 (5.1) eV and E_{act} is 94 kJ/mol, respectively. The peak positions in Figure 3 show that there are no alkali s-orbital contributions below the Fermi-level. We note that the alkali cation bands seem to overlap with those of ethylene, but the cation and ethylene are too spatially separated to interact.

The pDOS of the MY models shows no qualitative trend with the energy gaps for this type of system either. For instance, e_{norm} and e_{inv} in KY and RbY are similar, but the activation energies differ with 34 kJ/mol.

The most significant band overlap between the alkali cation and DMF is found for NaY and RbY. In the former the $LUMO_{DMF}$ interacts with the LUMO+1 of Na^+. In the latter, $LUMO_{DMF}$ interacts with the LUMO of Rb^+. However, the ICOOP-analysis yields values of −0.61 and −0.41, respectively, indicating net antibonding orbital interaction between the cations and O_{DMF}. Furthermore, the interaction between the cation and the carbon backbone of the DMF furan ring is also antibonding with ICOOP values of −0.05 and −0.12 in NaY and RbY, respectively. For reference, ICOOP of C−C bonds reach +0.36; see also Table 1. From the data presented here we infer that changes to the DAC reaction barrier cannot be

Table 1. Integrated COHP and COOP Values for Selected Interatomic Interactions[a]

	ICOHP (ICOOP) $O_{DMF}\cdots$SII	ICOHP (ICOOP) $O_{DMF}\cdots$SIII	$\sum$ICOHP $O_{DMF}\cdots$M (A)	ICOHP (ICOOP) $M\cdots C_{DMF}$ (B)	ratio A/B	ICOHP (ICOOP) C1$\cdots$C6	ICOHP (ICOOP) C4$\cdots$C5
1/LiY	−0.07 (−0.01)	−2.51 (0.10)	−2.58	−1.19 (−0.13)	2.17	0.00 (0.00)	0.00 (0.00)
TS1/LiY	−0.06 (−0.01)	−2.83 (0.12)	−2.89	−1.10 (−0.10)	2.62	−1.98 (0.11)	−1.84 (0.11)
2/LiY	−0.06 (−0.02)	−3.36 (0.17)	−3.42	−1.06 (−0.09)	3.24	−7.97 (0.36)	−8.00 (0.36)
1/NaY	−0.03 (0.00)	−0.57 (0.03)	−0.61	−0.27 (−0.05)	2.25	0.00 (0.00)	−0.01 (0.00)
TS1/NaY	−0.07 (0.00)	−0.63 (0.03)	−0.70	−0.27 (−0.04)	2.58	−1.91 (0.11)	−2.05 (0.12)
2/NaY	−0.14 (0.01)	−0.73 (0.03)	−0.87	−0.29 (−0.05)	2.95	−7.76 (0.36)	−7.79 (0.36)
1/KY	−0.14 (0.00)	−0.31 (0.01)	−0.45	−0.26 (−0.11)	1.71	0.00 (0.00)	0.00 (0.00)
TS1/KY	−0.20 (0.00)	−0.33 (0.01)	−0.53	−0.24 (−0.10)	2.26	−2.07 (0.12)	−2.04 (0.11)
2/KY	−0.28 (0.02)	−0.38 (0.01)	−0.67	−0.26 (−0.10)	2.58	−7.78 (0.36)	−7.73 (0.35)
1/RbY	−0.17 (−0.00)	−0.24 (0.01)	−0.41	−0.25 (−0.12)	1.61	−0.01 (0.00)	−0.01 (0.00)
TS1/RbY	−0.19 (0.00)	−0.27 (0.01)	−0.46	−0.21 (−0.10)	2.22	−2.13 (0.12)	−2.09 (0.12)
2/RbY	−0.27 (0.01)	−0.31 (0.01)	−0.58	−0.22 (−0.09)	2.62	−7.85 (0.36)	−7.86 (0.36)
1/CsY	−0.11 (−0.01)	−0.16 (0.01)	−0.27	−0.17 (−0.10)	1.55	0.00 (0.00)	−0.01 (0.00)
TS1/CsY	−0.14 (−0.01)	−0.17 (0.00)	−0.32	−0.16 (−0.09)	2.00	−2.05 (0.11)	−2.07 (0.12)
2/CsY	−0.20 (−0.01)	−0.21 (−0.01)	−0.41	−0.17 (−0.06)	2.45	−7.91 (0.36)	−7.86 (0.36)

[a]The ICOOP values are shown in-between brackets. Positive ICOOP values indicate net bonding interactions whereas negative ICOOP values indicate net anti-bonding interactions.

ascribed to Lewis acid catalysis via interactions between the cations s-orbitals and reactant FMOs.

3.3. Electron Density Analysis. Because our periodic MY models are chemically the most representative models as compared to the MFAU isolated site models, we focus on analyzing the MY systems in greater detail. KY and RbY are systems of primary interest, although they will sometimes be referenced to other MY systems. KY is chosen, as we have shown that it is the most active catalyst among a set of alkali-exchanged FAU zeolites.[36] RbY is chosen, as it is the most confined system, illustrated by the shortest $C_1\cdots C_6/C_4\cdots C_5$ distances of the IS. Any confinement-driven interaction or feature that is lacking in RbY is assumed not to be found in any other MY system studied in this work.

Activated Reactant Complex. To analyze the intermolecular interactions in the IS between DMF and ethylene, we determined the atomic net charges and the properties of the electron density. Such properties are the Laplacian and the electron density at the bond critical points. The DMF and ethylene net molecular charges are reported in Figure 4 and Tables S1. These results were complemented by the bond-order analysis, performed to study the evolution of the $C_1\cdots C_6/C_4\cdots C_5$ bonds over the course of the reaction, Figure 5.

The net molecular charges in Figure 4 are obtained by summing all atomic net charges belonging to the all atoms part of the molecule. Note that when referring to ethylene in the TS
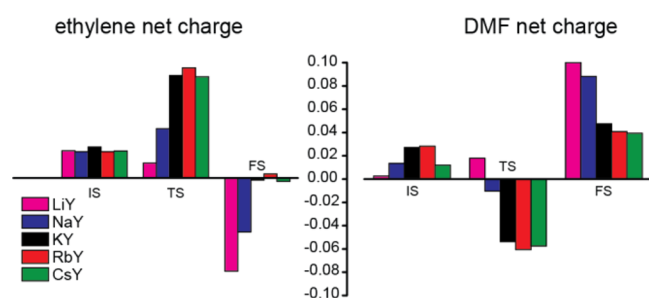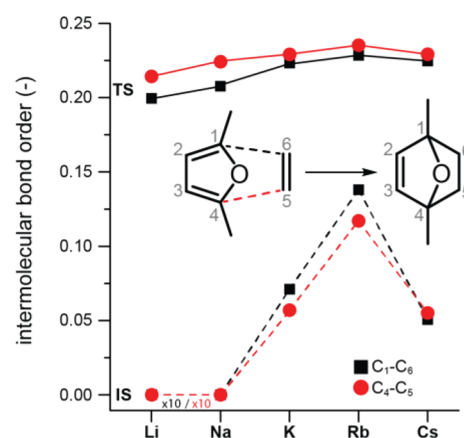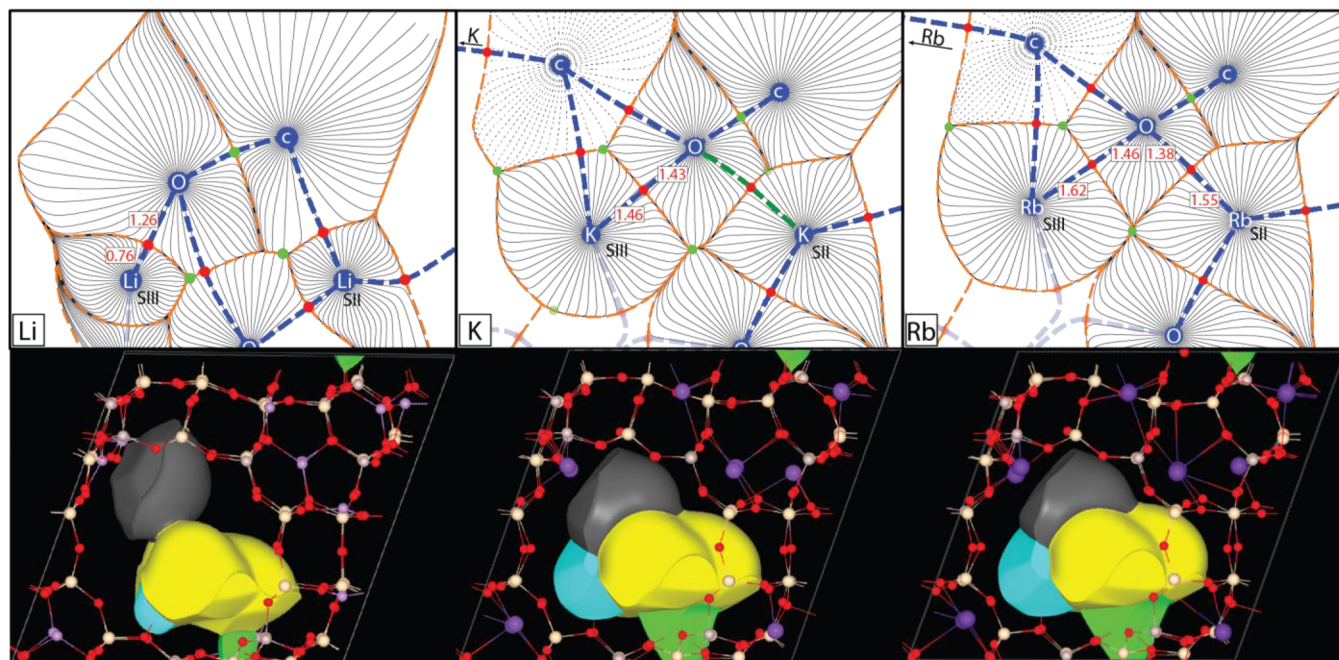

Figure 5. Evolution of the intramolecular bond orders in the DAC reaction between DMF and ethylene over MY. The final state is omitted. Note that the bond orders in the IS are 1 order of magnitude smaller.
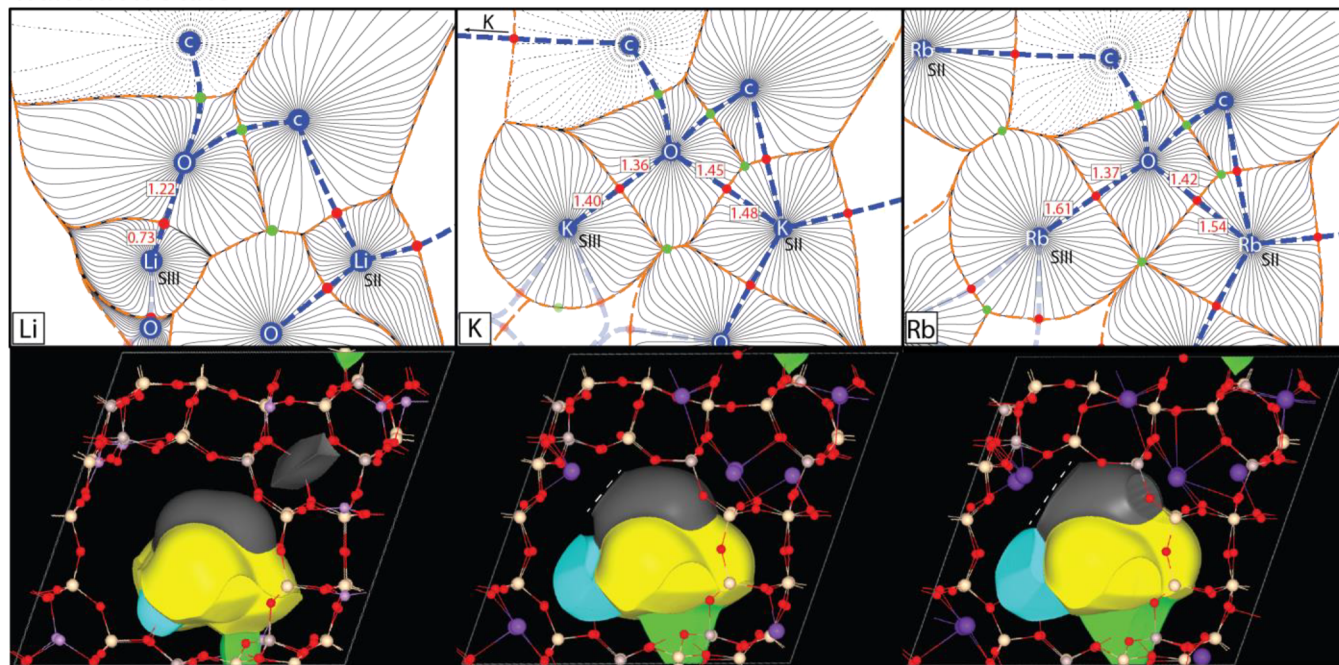
or FS, we actually refer to the two methylene moieties originating from ethylene. Inspection of Figure 4 shows that the molecular net charges are typically low ($|\Delta q| < 0.1$). Furthermore, the net charge of ethylene typically cancels that of DMF in the TS and FS. A minor imbalance is found in **TS1**/RbY, amounting to −0.04 e⁻. This net charge is considered insignificant and is believed to arise from asymmetric interactions with the framework. Furthermore, if charge transfer occurs to the zeolite matrix at all, it is considered too small to account for the large DAC reaction barrier reduction.

The electron density and the Laplacian values at the BCPs were compared for **1**/KY and **1**/RbY. The BCP-analysis indicates that there is no difference between **1**/KY and **1**/RbY. That is, both systems lack BCPs between the C1$\cdots$C6 and C4$\cdots$C5 atom pairs in the IS. Only upon formation of either **TS1**/KY or **TS1**/RbY, C1$\cdots$C6 and C4$\cdots$C5 BCPs are observed with electron densities of 0.46 e⁻/Bohr³, and Laplacians ranging from 0.64 to 0.69. To put this in perspective, a C1−C6 or C4−C5 bond in both **2**/KY and

Figure 4. DMF and ethylene net charges. Note that "ethylene" in the TS and FS refers to the two methylene moieties initially belonging to ethylene.

Figure 6. Topological analysis of the electron density and molecular basins of selected cations and reactants. Atom colors are red = O, beige = Si, light or dark purple = alkali cation. Yellow basin = DMF, gray basin = ethylene, light blue basin = cation at SIII site, light green basin = cation at SII site. The white dashed line is meant to guide the eye.

2/RbY has an electron density of 1.57 e⁻/Bohr³ with a Laplacian of ca. −12.7.

The BO-analysis (Figure 5) yielded only significant bond orders for **1**/KY, **1**/RbY, and **1**/CsY for the C1···C6 and C4···C5 atom pairs, albeit small. Values are zero for LiY and NaY and reach a maximum of 0.014 for RbY. Formation of **TS1**

results in the appearance of partial bonds: the BO of the C1−C6 pair gradually increases from 0.2 to 0.229 (LiY to RbY) while the bond order of (C1···C6)$_{CsY}$ is 0.225. The BO of the C4···C5 atom pair increases from 0.214 to 0.235 (LiY to RbY) with the bond order of (C4···C5)$_{CsY}$ being 0.23. The error in our work is believed to be 0.01. The appearance of a trend in

the BO of the IS- and TS-BO in Figure 5 is consistent with the increasing cation radius, noting that ethylene in **1**/CsY is located at a different position.

In summary, the DAC reaction occurs in a charge-neutral fashion with a bidirectional electron flow, in line with earlier findings using isolated site models.[71] Additionally, we do not believe that the cations induce significant changes to the intermolecular charge transfer. The Laplacians indicate slight interactions between DMF and C_2H_4 in the IS. This is supported by the BO-analysis. These results qualitatively connect with our earlier hypothesis on IS destabilization.

Zeolite–Reactant Interactions. To understand the exact role of the exchangeable cations in the zeolite, we studied the interaction of the cations at the SII and SIII sites with the furanic oxygen atom (O_{DMF}) in greater depth. We refer to the cation–furanic oxygen interactions as O_{DMF}···SII and O_{DMF}···SIII, respectively. The SII cation can also interact with the π-system of the DMF carbon backbone. This consists of the four carbon atoms in the furanic five-membered ring, grouped into a term we refer to as C_{DMF}. We refer to the cation–carbon backbone interaction as the SII–C_{DMF} interaction. We exclude the methyl side groups. BCPs of the aforementioned interactions have been analyzed (Figure 6, Table S2, and Figure S3) and were complemented by the results of the COHP-analysis (Table 1).

In **1**/LiY and **1**/NaY, a BCP for the O_{DMF}···SII interaction is absent. Additionally, BO-values are only 0.001 in LiY and NaY. This indicates a lack of O_{DMF}···SII interaction. In **1**/KY, the BO is 0.034, but no BCP was detected. We attribute this to the magnitude of the electron density being below our analysis threshold, whereas no threshold is set for the BO-analysis.

In contrast, the BOs of O_{DMF}···SII in **1**/RbY and **1**/CsY are 0.057 and 0.04, respectively. In addition, BCPs are found with electron densities of 0.101 e^-/bohr^3 and 0.064 e^-/bohr^3 for **1**/RbY and **1**/CsY, respectively. The Laplacians are 1.617 and 0.917, respectively.

An O_{DMF}···SIII interaction is always present in **1**/MY. This is no surprise, as the cation at the SIII site is the most accessible cation. Yet, BOs are generally low, varying between 0.097 and 0.061 in **1**/LiY and **1**/CsY, respectively. Upon reaching the transition state, the O_{DMF}···SIII BO typically increases with a ΔBO of ca. 0.015–0.02 in all MY. The electron densities at the BCPs in the IS of **1**/LiY and **1**/CsY are 0.164 and 0.042 e-/bohr^3, respectively. These BCPs have Laplacians of 3.677 to 0.534, respectively.

The positive values of the Laplacians and the relatively low electron density at the BCPs are indicative of ionic interactions between the cations and the furanic oxygen atom. This is in line with the antibonding orbital interactions found earlier.

We performed the COHP-analysis to quantify the interaction strengths. We note that the ICOHP should be interpreted with care,[72,73] because no direct comparison between different systems is possible. For instance, the O_{DMF}···SIII interaction strength cannot be plotted as a function of the cation. The studied systems have different total energies and very different chemical compositions so that the reference is not the same. Different models can only be compared by looking at ratios between the different components within every system.

Table 1 lists the ICOHP and ICOOP results for each state (IS, TS, FS) and for each alkali cation. The ratio between the $\sum$ICOHP(O_{DMF}···M) and ICOHP(M···C_{DMF}) is of interest. The cation–oxygen interactions are found to be dominant.

This is most clear in **2**/LiY and **2**/NaY, for which the cumulative oxygen–cation interaction is found to be 3.24 and 2.95 times stronger than the C_{DMF}···M interaction, respectively. The same ratios range from 1.55 to 1.71 in KY, RbY, and CsY. Thus O_{DMF}···M electrostatic interactions dominate the overall interaction between the reactants and the alkali-exchanged faujasite catalyst.

3.4. Topological Analysis of the Electron Density. The selected results of the topological analyses of the electron density for the initial and transition states formed with LiY, KY, and RbY are shown in Figure 6. The more extensive data including the respective isosurfaces are included in Supporting Information, Figure S3. Atomic basins are visualized by the dashed yellow lines. The in-plane bond-paths are referred to as bond-path type I and are depicted as dashed blue lines. BCPs are shown with red dots. A dashed green line is referred to as bond-path type II and represents an out-of-plane bond-path between the SII cation and a carbon atom of the DMF methyl side group. Green dots represent ring-critical points. The bond-path between the SII-cation and one of the C-atoms of either the ethylene double bond or DMF C2/C3 bond is actually out-of-plane. Minor fluctuations in the electron density are believed to be responsible for lacking the second bond-path between the SII-cation and the other C-atom. This is supported by the bond-path showing a tendency to bifurcate in the 3D-visualization (data not shown). Thus, we envisage that the bond-path could potentially have been drawn between the SII-cation and the other C-atom of the aforementioned bonds as well (e.g., ethylene coordination to SII is highly symmetric). We interpreted this as an in-plane cation–π interaction and consequently projected the bond-path onto the plane.

The red numbers are hypervector lengths (Å) between an atom and the BCP. Their lengths are summarized in Table S3. The molecular basins have been plotted by summing the atomic basins present in either of the reactants. Thus, the yellow and gray volumes represent DMF and ethylene, respectively. The light blue and light green volumes represent the SIII and SII cations, respectively.

The projections show that ethylene and DMF already interact relatively significant in **1**/KY and **1**/RbY as compared to **1**/LiY. We also note the flat surface (white dashed line) near the SII cation to which ethylene was initially adsorbed in **TS1**/KY and **TS1**/RbY. This is completely absent in the case of LiY.

Upon comparing every pair of hypervectors that belong to the same bond-path, we find that the length becomes increasingly similar upon increasing alkali cation radius. This is most pronounced in the final state, to a lesser degree in the transition state, and least in the initial state. We ascribe this to the increasing cation radius. Analysis of **1**/RbY and **TS1**/RbY in Figure 6 illustrates the practically equal total hypervector lengths between SII···O_{DMF} and SIII···O_{DMF}. Additionally, the changes in hypervector length are smallest for RbY. That is, hypervectors in **1** → **TS1** and **TS1** → **2** change with 0.03 (0.1) and 0.06 (0.04) Å for SII···O_{DMF} (SIII···O_{DMF}). In the Cs⁺-exchanged Y zeolite, changes in **TS1** → **2** are 0.05 and 0.15 Å for SII···O_{DMF} and SIII···O_{DMF}, respectively.

To conclude, we measured the SII···O_{DMF} and SIII···O_{DMF} distances present in the obtained geometries (Table 2). Reflecting these on the M–O distances found in alkali oxides,[74] we find that SII···O_{DMF} and SIII···O_{DMF} in **TS1**/RbY mimic the alkali oxide M–O distances best.

Table 2. Interatomic Distances (Å) in the TS As Measured for MY Models

	LiY	NaY	KY	RbY	CsY
$d(\text{SII}\cdots\text{O})$	3.67	3.26	2.92	2.96	3.21
$d(\text{SIII}\cdots\text{O})$	1.96	2.30	2.77	2.98	3.31
Δd	1.71	0.96	0.15	−0.02	−0.10
$d(\text{O}^{2-}\cdots\text{M}^+)^a$	2.16	2.42	2.78	2.92	3.07

^{a}Data adopted from ref 74.

In summary, Figure 6 and Figure S3 clearly show increased confinement in RbY as compared to LiY. The changes in SII···O$_{DMF}$ and SIII···O$_{DMF}$ distances along the reaction coordinate are the smallest in RbY. The RbY cation−O$_{DMF}$ distances resemble those found in rubidium oxide.

4. CONCLUSION

We have performed a periodic density functional theory study on the Diels−Alder Cycloaddition between DMF and ethylene over alkali-exchanged faujasites. Two models were studied; one resembled the isolated site model and one model contained a high density of accessible active sites.

The origin of the DAC-reactivity trend inversion in MY as compared to MFAU has been investigated with a wide variety of electronic structure analysis tools. We computed the atomic charges and performed the topological analysis of the electron density in conformity with the quantum theory of atoms in molecules, obtained bond orders using the density-derived electrostatic and chemical method (DDEC6), and investigated pairwise interatomic interactions with the crystal orbital Hamilton population (COHP) and crystal orbital overlap population (COOP) analysis.

The results show confinement-driven reactivity characterized by initial-state destabilization upon increasing cation size, most pronounced in RbY. In all studied systems, multisite cooperativity stabilizes the transition state via ionic interactions. Cation−reactant orbital interactions are insignificant and are of net antibonding nature in the evaluated MY models. Changes to the geometry of the reactive complex are smallest in RbY. The furanic oxygen−cation interatomic distances are most symmetric and closely resemble that of rubidium oxide. The combination of these effects is the cause of the DAC-reactivity trend inversion, with the lowest barrier found for RbY. These results illustrate the importance of confinement-driven reactivity and multisite cooperativity in alkali-exchanged zeolite catalysis.

■ ASSOCIATED CONTENT

ⓈSupporting Information

The Supporting Information is available free of charge on the ACS Publications website at DOI: 10.1021/acs.jpcc.8b04409.

> Computational details of QTAIM-theory-based analysis; details on the COHP and COOP analysis; DFT-computed DMF and ethylene adsorption energies and DAC-activation energy; exemplary COOP-plots of NaY and RbY; supplementary results of the BCP-analysis based on the QTAIM-theory; topological analysis and 3D visualization of the electron density (PDF)

■ AUTHOR INFORMATION

Corresponding Authors

*E-mail: e.j.m.hensen@tue.nl.

*E-mail: e.a.pidko@tudelft.nl.

ORCID ⃝

Roderigh Y. Rohling: 0000-0002-4789-8896

Emiel J. M. Hensen: 0000-0002-9754-2417

Evgeny A. Pidko: 0000-0001-9242-9901

Present Address

∥Current address: Inorganic Systems Engineering group, Department of Chemical Engineering, Faculty of Applied Sciences, Delft University of Technology, Van der Maasweg 9, 2629 HZ Delft, The Netherlands.

Author Contributions

§These authors contributed equally to the manuscript.

Notes

The authors declare no competing financial interest.

■ ACKNOWLEDGMENTS

■ REFERENCES

(1) Diels, O.; Alder, K. Synthesen in der Hydroaromatischen Reihe. *Leibigs Ann. Chem.* **1928**, *460*, 98−122.

(2) Tasdelen, M. A. Diels−Alder "click" Reactions: Recent Applications in Polymer and Material Science. *Polym. Chem.* **2011**, *2*, 2133−2145.

(3) Heravi, M. M.; Ahmadi, T.; Ghavidel, M.; Heidari, B.; Hamidi, H. Recent Applications of the Hetero Diels−Alder Reaction in the Total Synthesis of Natural Products. *RSC Adv.* **2015**, *5*, 101999−102075.

(4) Nicolaou, K. C.; Snyder, S. a.; Montagnon, T.; Vassilikogiannakis, G. The Diels - Alder Reaction in Total Synthesis. *Angew. Chem., Int. Ed.* **2002**, *41*, 1668.

(5) Kappe, C. O.; Murphree, S. S.; Padwa, A. Synthetic Applications of Furan Diels-Alder Chemistry. *Tetrahedron* **1997**, *53*, 14179−14233.

(6) Funel, J.-A.; Abele, S. Industrial Applications of the Diels-Alder Reaction. *Angew. Chem., Int. Ed.* **2013**, *52*, 3822−3863.

(7) Houk, K. N.; Gonzalez, J.; Li, Y. Pericyclic Reaction Transition States: Passions and Punctilios, 1935−1995. *Acc. Chem. Res.* **1995**, *28*, 81−90.

(8) Houk, K. N.; Li, Y.; Evanseck, J. D. Transition Structures of Hydrocarbon Pericyclic Reactions. *Angew. Chem., Int. Ed. Engl.* **1992**, *31*, 682−708.

(9) Domingo, L. R.; José Aurell, M.; Pérez, P.; Contreras, R. Origin of the Synchronicity on the Transition Structures of Polar Diels-Alder Reactions. Are These Reactions [4 + 2] Processes? *J. Org. Chem.* **2003**, *68*, 3884−3890.

(10) Fukui, K.; Fujimoto, H. The Stereoselection Rule for Electrocyclic Interactions. *Bull. Chem. Soc. Jpn.* **1967**, *40*, 2018−2025.

(11) Fukui, K.; Fujimoto, H. An MO-Theoretical Interpretation of the Nature of Chemical Reactions. II. The Governing Principles. *Bull. Chem. Soc. Jpn.* **1969**, *42*, 3399−3409.

(12) Fukui, K. Recognition of Stereochemical Paths by Orbital Interaction. *Acc. Chem. Res.* **1971**, *4*, 57−64.

(13) Houk, K. N. The Frontier Molecular Orbital Theory of Cycloaddition Reactions. *Acc. Chem. Res.* **1975**, *8*, 361−369.

(14) Ess, D. H.; Jones, G. O.; Houk, K. N. Conceptual, Qualitative, and Quantitative Theories of 1,3-Dipolar and Diels-Alder Cycloadditions Used in Synthesis. *Adv. Synth. Catal.* **2006**, *348*, 2337−2361.

(15) Hoffmann, R.; Woodward, R. B. Selection Rules for Concerted Cycloaddition Reactions. *J. Am. Chem. Soc.* **1965**, *87*, 2046−2048.

(16) Hoffmann, R.; Woodward, R. B. The Conservation of Orbital Symmetry. *Acc. Chem. Res.* **1968**, *1*, 17−22.

(17) Sauer, J.; Sustmann, R. Mechanistic Aspects of Diels-Alder Reactions - a Critical Survey. *Angew. Chem., Int. Ed. Engl.* **1980**, *19*, 779−807.

(18) Kiselev, V. D.; Konovalov, A. I. Internal and External Factors Influencing the Diels-Alder Reaction. *J. Phys. Org. Chem.* **2009**, *22*, 466−483.

(19) Domingo, L. R.; Sáez, J. a. Understanding the Mechanism of Polar Diels-Alder Reactions. *Org. Biomol. Chem.* **2009**, *7*, 3576−3583.

(20) Houk, K. N. Generalized Frontier Orbitals of Alkenes and Dienes. Regioselectivity in Diels-Alder Reactions. *J. Am. Chem. Soc.* **1973**, *95*, 4092−4094.

(21) Branchadell, V.; Sodupe, M.; Ortuño, R. M.; Oliva, A.; Gomez-Pardo, D.; Guingant, A.; D'Angelo, J. Diels-Alder Cycloadditions of Electron-Rich, Electron-Deficient, and Push-Pull Dienes with Cyclic Dienophiles: High-Pressure-Induced Reactions and Theoretical Calculations. *J. Org. Chem.* **1991**, *56*, 4135−4141.

(22) Fringuelli, F.; Piermatti, O.; Pizzo, F.; Vaccaro, L. Recent Advances in Lewis Acid Catalyzed Diels−Alder Reactions in Aqueous Media. *Eur. J. Org. Chem.* **2001**, *2001*, 439−455.

(23) Çelebi-Ölçüm, N.; Ess, D. H.; Aviyente, V.; Houk, K. N. Effect of Lewis Acid Catalysts on Diels−Alder and Hetero-Diels−Alder Cycloadditions Sharing a Common Transition State. *J. Org. Chem.* **2008**, *73*, 7472−7480.

(24) Kumar, A. Salt Effects on Diels − Alder Reaction Kinetics. *Chem. Rev.* **2001**, *101*, 1−20.

(25) Yoshizawa, M.; Tamura, M.; Fujita, M. Diels-Alder in Aqueous Molecular. *Science* **2006**, *312*, 251−254.

(26) Inokuma, Y.; Yoshioka, S.; Fujita, M. A Molecular Capsule Network: Guest Encapsulation and Control of Diels-Alder Reactivity. *Angew. Chem., Int. Ed.* **2010**, *49*, 8912−8914.

(27) Heine, A.; Stura, E. A.; Yli-Kauhaluoma, J. T.; Gao, C.; Deng, Q.; Beno, B. R.; Houk, K. N.; Janda, K. D.; Wilson, I. A. An Antibody Exo Diels-Alderase Inhibitor Complex at 1.95 Angstrom Resolution. *Science* **1998**, *279*, 1934−1940.

(28) Siegel, J. B.; Zanghellini, A.; Lovick, H. M.; Kiss, G.; Lambert, A. R.; St. Clair, J. L.; Gallaher, J. L.; Hilvert, D.; Gelb, M. H.; Stoddard, B. L.; et al. Computational Design of an Enzyme Catalyst for a Stereoselective Bimolecular Diels-Alder Reaction. *Science* **2010**, *329*, 309−313.

(29) Hilvert, D.; Hill, K. W.; Nared, K. D.; Auditor, M. T. M. Antibody Catalysis of the Diels-Alder Reaction. *J. Am. Chem. Soc.* **1989**, *111*, 9261−9262.

(30) Xu, J.; Deng, Q.; Chen, J.; Houk, K. N.; Bartek, J.; Hilvert, D.; Wilson, I. A. Evolution of Shape Complementarity and Catalytic Efficiency from a Primordial Antibody Template. *Science* **1999**, *286*, 2345−2348.

(31) Narayan, S.; Muldoon, J.; Finn, M. G.; Fokin, V. V.; Kolb, H. C.; Sharpless, K. B. On Water": Unique Reactivity of Organic Compounds in Aqueous Suspension. *Angew. Chem., Int. Ed.* **2005**, *44*, 3275−3279.

(32) Blokzijl, W.; Blandamer, M. J.; Engberts, J. B. F. N. Diels-Alder Reactions in Aqueous Solutions. Enforced Hydrophobic Interactions between Diene and Dienophile. *J. Am. Chem. Soc.* **1991**, *113*, 4241−4246.

(33) Otto, S.; Blokzijl, W.; Engberts, J. B. F. N. Diels-Alder Reactions in Water. Effects of Hydrophobicity and Hydrogen Bonding. *J. Org. Chem.* **1994**, *59*, 5372−5376.

(34) Blokzijl, W.; Engberts, J. B. F. N. Initial-State and Transition-State Effects on Diels-Alder Reactions in Water and Mixed Aqueous Solvents. *J. Am. Chem. Soc.* **1992**, *114*, 5440−5442.

(35) Otto, S.; Engberts, J. B. F. N. Diels-Alder Reactions in Water. *Pure Appl. Chem.* **2000**, *72*, 1365−1372.

(36) Rohling, R. Y.; Uslamin, E.; Zijlstra, B.; Tranca, I. C.; Filot, I. A. W.; Hensen, E. J. M.; Pidko, E. A. An Active Alkali-Exchanged Faujasite Catalyst for *p*-Xylene Production via the One-Pot Diels−

(37) Rohling, R. Y.; Hensen, E. J. M.; Pidko, E. A. Multi-Site Cooperativity in Alkali-Metal-Exchanged Faujasites for the Production of Biomass-Derived Aromatics. *ChemPhysChem* **2018**, *19*, 446−458.

(38) Pidko, E. A.; Van Santen, R. A. Molecular Recognition in Cation-Exchanged Zeolites. *Int. J. Quantum Chem.* **2010**, *110*, 210−220.

(39) Nachtigall, P.; Delgado, M. R.; Nachtigallova, D.; Arean, C. O. The Nature of Cationic Adsorption Sites in Alkaline Zeolites—single, Dual and Multiple Cation Sites. *Phys. Chem. Chem. Phys.* **2012**, *14*, 1552−1569.

(40) Van Santen, R. A.; Tranca, I. How Molecular Is the Chemisorptive Bond? *Phys. Chem. Chem. Phys.* **2016**, *18*, 20868−20894.

(41) Van Santen, R. A. *Modern Heterogeneous Catalysis: An Introduction*; Wiley-VCH Verlag GmbH & Co. KGaA: Weinheim, Germany, 2017.

(42) Van Santen, R. A.; Tranca, I.; Hensen, E. J. M. Theory of Surface Chemistry and Reactivity of Reducible Oxides. *Catal. Today* **2015**, *244*, 63−84.

(43) Liu, C.; Tranca, I.; van Santen, R. A.; Hensen, E. J. M.; Pidko, E. A. Scaling Relations for Acidity and Reactivity of Zeolites. *J. Phys. Chem. C* **2017**, *121*, 23520−23530.

(44) Manz, T. A.; Limas, N. G. Introducing DDEC6 Atomic Population Analysis: Part 1. Charge Partitioning Theory and Methodology. *RSC Adv.* **2016**, *6*, 47771−47801.

(45) Limas, N. G.; Manz, T. A. Introducing DDEC6 Atomic Population Analysis: Part 2. Computed Results for a Wide Range of Periodic and Nonperiodic Materials. *RSC Adv.* **2016**, *6*, 45727−45747.

(46) Manz, T. A. Introducing DDEC6 Atomic Population Analysis: Part 3. Comprehensive Method to Compute Bond Orders. *RSC Adv.* **2017**, *7*, 45552−45581.

(47) Dronskowski, R.; Bloechl, P. E. Crystal Orbital Hamilton Populations (COHP): Energy-Resolved Visualization of Chemical Bonding in Solids Based on Density-Functional Calculations. *J. Phys. Chem.* **1993**, *97*, 8617−8624.

(48) Deringer, V. L.; Tchougréeff, A. L.; Dronskowski, R. Crystal Orbital Hamilton Population (COHP) Analysis as Projected from Plane-Wave Basis Sets. *J. Phys. Chem. A* **2011**, *115*, 5461−5466.

(49) Maintz, S.; Deringer, V. L.; Tchougréeff, A. L.; Dronskowski, R. Analytic Projection from Plane-Wave and PAW Wavefunctions and Application to Chemical-Bonding Analysis in Solids. *J. Comput. Chem.* **2013**, *34*, 2557−2567.

(50) Maintz, S.; Deringer, V. L.; Tchougréeff, A. L.; Dronskowski, R. LOBSTER: A Tool to Extract Chemical Bonding from Plane-Wave Based DFT. *J. Comput. Chem.* **2016**, *37*, 1030−1035.

(51) Maintz, S.; Esser, M.; Dronskowski, R. Efficient Rotation of Local Basis Functions Using Real Spherical Harmonics. *Acta Phys. Pol., B* **2016**, *47*, 1165.

(52) Hoffmann, R. Interaction of Orbitals through Space and through Bonds. *Acc. Chem. Res.* **1971**, *4*, 1−9.

(53) Tang, W.; Sanville, E.; Henkelman, G. A Grid-Based Bader Analysis Algorithm without Lattice Bias. *J. Phys.: Condens. Matter* **2009**, *21*, 84204.

(54) Sanville, E.; Kenny, S. D.; Smith, R.; Henkelman, G. Improved Grid-Based Algorithm for Bader Charge Allocation. *J. Comput. Chem.* **2007**, *28*, 899−908.

(55) Henkelman, G.; Arnaldsson, A.; Jónsson, H. A Fast and Robust Algorithm for Bader Decomposition of Charge Density. *Comput. Mater. Sci.* **2006**, *36*, 354−360.

(56) Yu, M.; Trinkle, D. R. Accurate and Efficient Algorithm for Bader Charge Integration. *J. Chem. Phys.* **2011**, *134*, 64111.

(57) Bader, R. F. W. Atoms in Molecules: A Quantum Theory. *Atoms in Molecules: A Quantum Theory*; Clarendon Press: Oxford, 1994.

(58) Kresse, G.; Hafner, J. Ab Initio Molecular-Dynamics Simulation of the Liquid-Metal−amorphous-Semiconductor Transition in Germanium. *Phys. Rev. B: Condens. Matter Mater. Phys.* **1994**, *49*, 14251−14269.

(59) Kresse, G.; Furthmüller, J. Efficient Iterative Schemes for Ab Initio Total-Energy Calculations Using a Plane-Wave Basis Set. *Phys. Rev. B: Condens. Matter Mater. Phys.* **1996**, *54*, 11169−11186.

(60) Kresse, G.; Furthmüller, J. Efficiency of Ab-Initio Total Energy Calculations for Metals and Semiconductors Using a Plane-Wave Basis Set. *Comput. Mater. Sci.* **1996**, *6*, 15−50.

(61) Kresse, G.; Joubert, D. From Ultrasoft Pseudopotentials to the Projector Augmented-Wave Method. *Phys. Rev. B: Condens. Matter Mater. Phys.* **1999**, *59*, 1758−1775.

(62) Kresse, G.; Hafner, J. Ab Initio Molecular Dynamics for Liquid Metals. *Phys. Rev. B: Condens. Matter Mater. Phys.* **1993**, *47*, 558−561.

(63) Grimme, S.; Antony, J.; Ehrlich, S.; Krieg, H. A Consistent and Accurate Ab Initio Parametrization of Density Functional Dispersion Correction (DFT-D) for the 94 Elements H-Pu. *J. Chem. Phys.* **2010**, *132*, 154104.

(64) Grimme, S.; Ehrlich, S.; Goerigk, L. Effect of the Damping Function in Dispersion Corrected Density Functional Theory. *J. Comput. Chem.* **2011**, *32*, 1456−1465.

(65) Henkelman, G.; Uberuaga, B. P.; Jónsson, H. A Climbing Image Nudged Elastic Band Method for Finding Saddle Points and Minimum Energy Paths. *J. Chem. Phys.* **2000**, *113*, 9901−9904.

(66) Henkelman, G.; Jónsson, H. Improved Tangent Estimate in the Nudged Elastic Band Method for Finding Minimum Energy Paths and Saddle Points. *J. Chem. Phys.* **2000**, *113*, 9978−9985.

(67) Vega, D.; Almeida, D. AIM-UC: An Application for QTAIM Analysis. *J. Comput. Methods Sci. Eng.* **2014**, *14*, 131−136.

(68) Custodio, L.; Etiene, T.; Pesco, S.; Silva, C. Practical Considerations on Marching Cubes 33 Topological Correctness. *Comput. Graph.* **2013**, *37*, 840−850.

(69) *The Quantum Theory of Atoms in Molecules: From Solid State to DNA and Drug Design*; Matta, F. C., Boyd, J. R., Eds.; Wiley-VCH Verlag GmbH & Co. KGaA: Weinheim, Germany, 2007.

(70) Landrum, G. A.; Dronskowski, R. The Orbital Origins of Magnetism: From Atoms to Molecules to Ferromagnetic Alloys. *Angew. Chem., Int. Ed.* **2000**, *39*, 1560−1585.

(71) Nikbin, N.; Feng, S.; Caratzoulas, S.; Vlachos, D. G. P- Xylene Formation by Dehydrative Aromatization of a Diels−Alder Product in Lewis and Brønsted Acidic Zeolites. *J. Phys. Chem. C* **2014**, *118*, 24415−24424.

(72) Börnsen, N.; Meyer, B.; Grotheer, O.; Fähnle, M. E Cov - a New Tool for the Analysis of Electronic Structure Data in a Chemical Language. *J. Phys.: Condens. Matter* **1999**, *11*, L287−L293.

(73) Grechnev, A.; Ahuja, R.; Eriksson, O. Balanced Crystal Orbital Overlap Population - A Tool for Analysing Chemical Bonds in Solids. *J. Phys.: Condens. Matter* **2003**, *15*, 7751−7761.

(74) Shannon, R. D. Revised Effective Ionic Radii and Systematic Studies of Interatomic Distances in Halides and Chalcogenides. *Acta Crystallogr., Sect. A: Cryst. Phys., Diffr., Theor. Gen. Crystallogr.* **1976**, *32*, 751−767.